

PAPER • OPEN ACCESS

# Embrittlement of WCLL blanket and its fracture mechanical assessment




To cite this article: Jarir Aktaa *et al* 2023 *Nucl. Fusion* **63** 096016

View the [article online](#) for updates and enhancements.

## You may also like

- [Theoretical evaluation of the tritium extraction from liquid metal flows through a free surface and through a permeable membrane](#)  
F.R. Ugorri, B. Garcinuño, C. Moreno et al.
- [3D MHD analysis of prototypical manifold for liquid metal blankets](#)  
Simone Siriano, Fernando Roca Ugorri, Alessandro Tassone et al.
- [Magnetohydrodynamic velocity and pressure drop in manifolds of a WCLL TBM](#)  
C. Mistrangelo, L. Bühler, C. Koehly et al.

# Embrittlement of WCLL blanket and its fracture mechanical assessment

Jarir Aktaa<sup>1,\*</sup> , Ermile Gaganidze<sup>1</sup>, Gaetano Bongiovi<sup>2</sup>, Pietro Arena<sup>3</sup> ,  
Gandolfo Alessandro Spagnuolo<sup>4</sup> , Giacomo Aiello<sup>4</sup>, Pierluigi Chiovaro<sup>2</sup>  
and Christian Bachmann<sup>4</sup>

<sup>1</sup> Karlsruhe Institute of Technology (KIT), Institute for Applied Materials, Hermann-von-Helmholtz-Platz 1, 76344 Eggenstein-Leopoldshafen, Germany

<sup>2</sup> Department of Engineering, University of Palermo, Viale delle Scienze, Ed. 6, 90128 Palermo, Italy

<sup>3</sup> ENEA FSN-ING, C.R. Brasimone, 40032 Camugnano, BO, Italy

<sup>4</sup> EUROfusion—Programme Management Unit, Boltzmannstrasse 2, 85748 Garching, Germany

E-mail: [jarir.aktaa@kit.edu](mailto:jarir.aktaa@kit.edu)

Received 6 April 2023, revised 9 July 2023

Accepted for publication 21 July 2023

Published 4 August 2023



## Abstract

In the European fusion programme, the Water Cooled Lithium Lead breeding blanket (WCLL BB) uses EUROFER as a structural material cooled with water at temperatures between 295 °C–328 °C and a pressure of 155 bar. The WCLL BB will be significantly irradiated (>2 dpa), while some parts will not receive significant heat loads, e.g. the sidewalls or the back-supporting structures. The irradiation, together with the irradiation temperature of EUROFER below 350 °C, produces a shift of the ductile-to-brittle-transition temperature (DBTT) to levels above room temperature at neutron doses, causing material damage as low as 2–3 dpa. Even though the DBTT does not reach the operating temperature level, brittle/non-ductile fracture is a concern during in-vessel maintenance when the BB temperature is below the DBTT. Two loading scenarios were identified as severe in this respect: (i) re-pressurization of the WCLL BB cooling loop after in-vessel maintenance, and (ii) dead weight loads during lifting of the BB segment. The embrittlement of the WCLL BB was investigated by quantifying the local DBTT shift in its parts based on current knowledge of the embrittlement behaviour of EUROFER under neutron irradiation. Therefore, a suitable, not overly conservative procedure was derived considering dpa damage and transmuted helium effects. The results demonstrate the ability to identify the 3D spread of the severely embrittled zones in the structure whose impact on the structural integrity was assessed considering the risk of brittle/non-ductile fracture. Thereby, the fracture mechanics approach established in nuclear codes was applied assuming its applicability to EUROFER. The embrittled zones in the first wall (FW) and its sidewalls pass the criteria when assessing the relatively low stresses resulting from the coolant pressure. The assessment was then continued considering stresses appearing in the FW during maintenance, in particular, when lifting the BB segment and transporting it out of the vacuum vessel. In this context, the maximum tolerable flaw sizes were determined in a parameter study considering designs of the FW with different cooling channel wall thicknesses.

\* Author to whom any correspondence should be addressed.



Original content from this work may be used under the terms of the [Creative Commons Attribution 4.0 licence](https://creativecommons.org/licenses/by/4.0/). Any further distribution of this work must maintain attribution to the author(s) and the title of the work, journal citation and DOI.

Keywords: neutron irradiation, embrittlement, WCLL, breeding blanket, brittle/non-ductile fracture, fracture mechanical assessment

(Some figures may appear in colour only in the online journal)

## 1. Introduction

Cooling DEMO In-Vessel Components made of EUROFER with water is an option followed in the European fusion programme. In particular, the Water Cooled Lithium Lead (WCLL) Breeding Blanket (BB) uses water cooling at pressurised water reactor conditions (295 °C–328 °C @ 15.5 MPa) [1, 2]. This means that a large part of the structure is subjected to high neutron fluence at relatively low irradiation temperatures (below  $\approx 350$  °C). This condition is, in particular, critical for the first wall (FW) channels that present lower temperatures at contact with water and higher values of dpa. It is known that at such temperatures the ductile-to-brittle-transition temperature (DBTT) of EUROFER shifts to levels above room temperature (RT) already at neutron doses, causing material damage as low as 2–3 dpa [3, 4]. In addition, He-transmutation enhances the total embrittlement amplifying this issue. Hence, it is expected that a large part of EUROFER present in the FW of the blanket will work in brittle conditions when it is cooled down to RT.

Even if the DBTT does not reach the operating temperature level, there is the concern that loads appearing during cooling down, e.g. pressure load, during maintenance, and/or re-pressurization of the WCLL cooling loop will cause fracture of the BB, since, in these moments, parts of it are at a temperature below the DBTT.

The aim of this study is to assess embrittlement in the WCLL blanket structure during plasma operation identifying critically embrittled parts/regions that would be at temperatures below the DBTT when cooling down the component and to carry out fracture mechanical assessment of the most critical parts of the WCLL blanket considering embrittled EUROFER material properties at RT and applying the major loads appearing during cooling down, maintenance, and/or re-pressurization of the WCLL cooling loop. The assessment is performed according to the rules of existing design criteria. Awaiting missing data, conservative estimations are assumed. Thereby, the loads that can be tolerated and/or should be managed during shutdown, maintenance and re-pressurization are estimated.

## 2. Embrittlement of the WCLL blanket

For the assessment of embrittlement in the WCLL blanket structure during plasma operation, locally resolved dpa and He production rates as well as temperatures are required.

Due to the BB dimensions, this study has focussed on one of the most loaded WCLL BB areas, the equatorial region of the central outboard blanket (COB) segment. In particular, with reference to the WCLL BB design reported in

[5], the area between two consecutive horizontal stiffening plates (i.e. an elementary cell or slice) has been considered in this study.

The dpa and He production rates have been obtained by neutronics analysis adopting MCNP6.2 [6] along with the JEFF-3.2 transport cross-section libraries [7]. A 3D fully heterogeneous MCNP model of an equatorial toroidal-radial slice of the COB of DEMO 2018 design (equipped with a WCLL BB) has been set up exploiting the MCNP feature that allows us to perform calculations on Abaqus unstructured mesh (UM) geometry representations. Of course, the UM used for neutronic calculations is coarser than the mesh usually adopted for thermo-mechanical analyses, but this procedure naturally allows an easy coupling between nuclear and mechanical calculations. As far as boundary conditions are concerned, reflecting surfaces have been used both in the poloidal and toroidal direction, respectively [8, 9] to take into account the geometrical continuity in those directions. Regarding the neutron source modelling, in the DEMO reactor neutrons enter the blanket directly from the plasma or after scattering (albedo effect) [8, 10]. In order to simulate these DEMO irradiation conditions, a local neutron source for the aforementioned WCLL BB slice model has been defined as a planar surface that emits neutrons biased in energy and cosine. The results have then been normalized using a neutron yield of  $7.095 \times 10^{20} \text{ ns}^{-1}$ , which is related to the plasma flat-top phase and corresponds to a fusion power of 1998 MW.

With respect to the temperature field arising within the considered domain, a steady-state thermal analysis reproducing the DEMO flat-top scenario has been carried out [11]. Among the different breeding zone layouts presented in [11], the optimized one, named V0.6\_B, has been adopted in this study. Since the aforementioned model does not take into account the manifold region, a uniform temperature of 311.5 °C, corresponding to the average between inlet and outlet coolant temperatures, has been considered for this area.

To quantify embrittlement and the size of embrittled zones in the different parts, the shift in the DBTT ( $\Delta\text{DBTT}$ ) at each position  $x$  is calculated considering the shifts due to dpa damage and transmuted He, respectively:

$$\Delta\text{DBTT}(x) = \Delta\text{DBTT}_{\text{dpa}}(x) + \Delta\text{DBTT}_{\text{He}}(x). \quad (1)$$

This linear decomposition of the shift is the most obvious approach that has been followed to quantify the influence of transmuted He based on the available sparse database [4], the results of which are further used here. A similar approach has been considered by other researchers in this field, e.g. [12] for the same purpose, which however needs to be further verified and if necessary modified when the database and knowledge

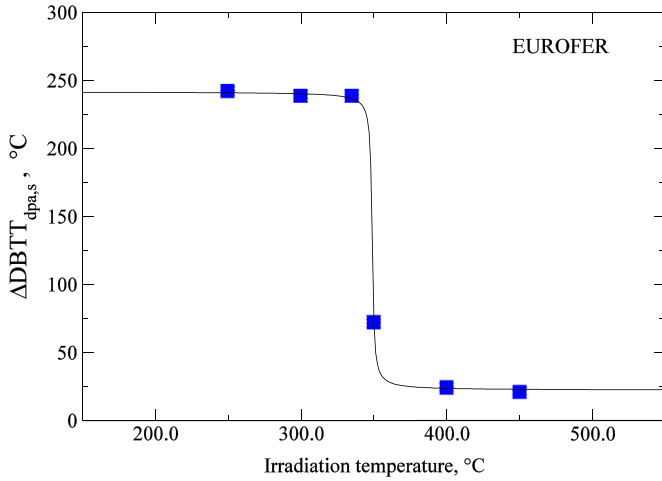


**Figure 1.** EUROFER's maximum possible DBTT shift due to dpa damage, estimated considering the experimentally determined DBTT shifts due to 16.3 dpa, versus irradiation temperature and its description by equation (3).

are sufficiently extended. For the determination of the shift due to dpa damage, the formula given in [13] for EUROFER is used:

$$\Delta\text{DBTT}_{\text{dpa}}(x) = \Delta\text{DBTT}_{\text{dpa,s}} \left( 1 - \exp\left(-\frac{\phi(x)}{\phi_0}\right) \right)^{1/2}. \quad (2)$$

$\phi(x)$  denotes the irradiation dose, which depends on the position and mainly varies in the radial direction. It is calculated by the irradiation dose rate  $\dot{\phi}(x)$  (in dpa/fpy) and the operation duration  $t_{\text{op}}$  (in fpy) to  $\phi(x) = \dot{\phi}(x)t_{\text{op}}$ .  $\Delta\text{DBTT}_{\text{dpa,s}}$  and  $\phi_0$  are temperature-dependent parameters and determined on the basis of available experimental data in the irradiation temperature range between 300 °C–330 °C to 238 °C and 16.7 dpa, respectively [13].  $\Delta\text{DBTT}_{\text{dpa,s}}$  denotes the maximum possible DBTT shift due to dpa damage. Its values at other temperatures are estimated presuming the validity of equation (2) with  $\phi_0$  independent of temperature and considering the same DBTT shifts due to 16.3 dpa at other irradiation temperatures [4, 13]. The resulting values, plotted as markers in figure 1, exhibit a stepwise transition within a narrow irradiation temperature range between 335 °C–350 °C from a high value at a lower temperature to a much smaller value at a higher temperature. Describing such behaviour, the following relation was found to fit fairly well with the estimated values of  $\Delta\text{DBTT}_{\text{dpa,s}}$  at different irradiation temperatures (see figure 1). By means of this relation, the value of  $\Delta\text{DBTT}_{\text{dpa,s}}$  can be determined at an arbitrary temperature  $T$  within the temperature range of interest:

$$\Delta\text{DBTT}_{\text{dpa,s}} = 132 - \frac{219.3}{\pi} \arctan(T - 348.85) \quad (3)$$

( $\Delta\text{DBTT}_{\text{dpa,s}}$  and  $T$  in °C).

For the additional shift due to transmuted He the irradiation temperature-dependent He embrittlement rate  $\Delta\text{DBTT}_1$  of EUROFER is considered, which denotes the mean value of DBTT shift due to 1 appm He. The values determined

by assessing the results of He simulation experiments, in particular, using a boron doping technique, e.g. [12, 14] or by spallation proton irradiation [15], lie between 0.15 and 0.25 °C/appm He dependent on irradiation temperature [4, 13]. While the lower value of 0.15 °C/appm He is conservatively estimated based on spallation target experiments for  $T < 380$  °C and up to 600 appm He, the upper value is determined based on boron doping experiments for temperatures around 450 °C and up to 432 appm He. Consequently, He embrittlement is worse at high irradiation temperatures (above 380 °C) and thus differs from embrittlement due to dpa. This can be explained by the increased mobility of He at high temperatures, which would enhance the formation of large clusters and even bubbles in configurations promoting fracture [16]. Hence, the dependence of  $\Delta\text{DBTT}_1$  on irradiation temperature within the temperature range of interest is described by a smooth stepwise function with transition at 380 °C using the following relation:

$$\Delta\text{DBTT}_1 = 0.2 - \frac{0.1}{\pi} \arctan(380 - T) \quad (4)$$

( $\Delta\text{DBTT}_1$  in °C/appm He and  $T$  in °C).

Hence, with  $\dot{G}_{\text{He}}$  as the He generation rate (in appm/fpy)  $\Delta\text{DBTT}_{\text{He}}(x)$  is calculated to be:

$$\Delta\text{DBTT}_{\text{He}}(x) = \Delta\text{DBTT}_1(T(x)) \dot{G}_{\text{He}}(x) t_{\text{op}}. \quad (5)$$

$\dot{G}_{\text{He}}$  depends not only on the neutron dose, but also on their energy and since the neutrons in the wall are slowed down the deeper they penetrate, it is a function of the location  $x$ . With equation (5), He embrittlement is assumed to be proportional to He production and does not show saturation as is the case for embrittlement due to dpa.

Following the procedure above, the total locally resolved DBTT shift can now be estimated for an arbitrary operation duration  $t_{\text{op}}$  provided the local operating temperature, dpa and He generation rates are known. Assuming  $t_{\text{op}} = 2$  fpy, this was conducted for the equatorial slice of the banana-shaped WCLL COB segment (see figure 2(a)), because of the higher neutron dose with respect to the other zones of the BB and for which the required input data are provided as fields (values at nodes for the corresponding Abaqus finite element mesh). In particular, these fields are imported into Abaqus (see figures 2(b)–(d)) and used in a user defined field subroutine to calculate the corresponding  $\Delta\text{DBTT}_{\text{dpa}}$ ,  $\Delta\text{DBTT}_{\text{He}}$  and  $\Delta\text{DBTT}$  as well as the DBTT using the equations above as fields depending on the operation time  $t_{\text{op}}$ . Hence, the fields can then be visualized and further evaluated utilizing the postprocessor Abaqus CAE. The contour plot of the DBTT field then allows the identification of critically embrittled regions for which the DBTT( $t_{\text{op}}$ ) is higher than the RT.

In figure 3, the  $\Delta\text{DBTT}_{\text{dpa}}$ ,  $\Delta\text{DBTT}_{\text{He}}$  and DBTT fields as well as the critically embrittled regions after  $t_{\text{op}} = 2$  fpy are illustrated, respectively, showing that large regions in the FW are critically embrittled. In particular, those that operate at relatively low temperatures ( $< 350$  °C) and not far away from its plasma-facing front. Indeed, it is interesting to note that the

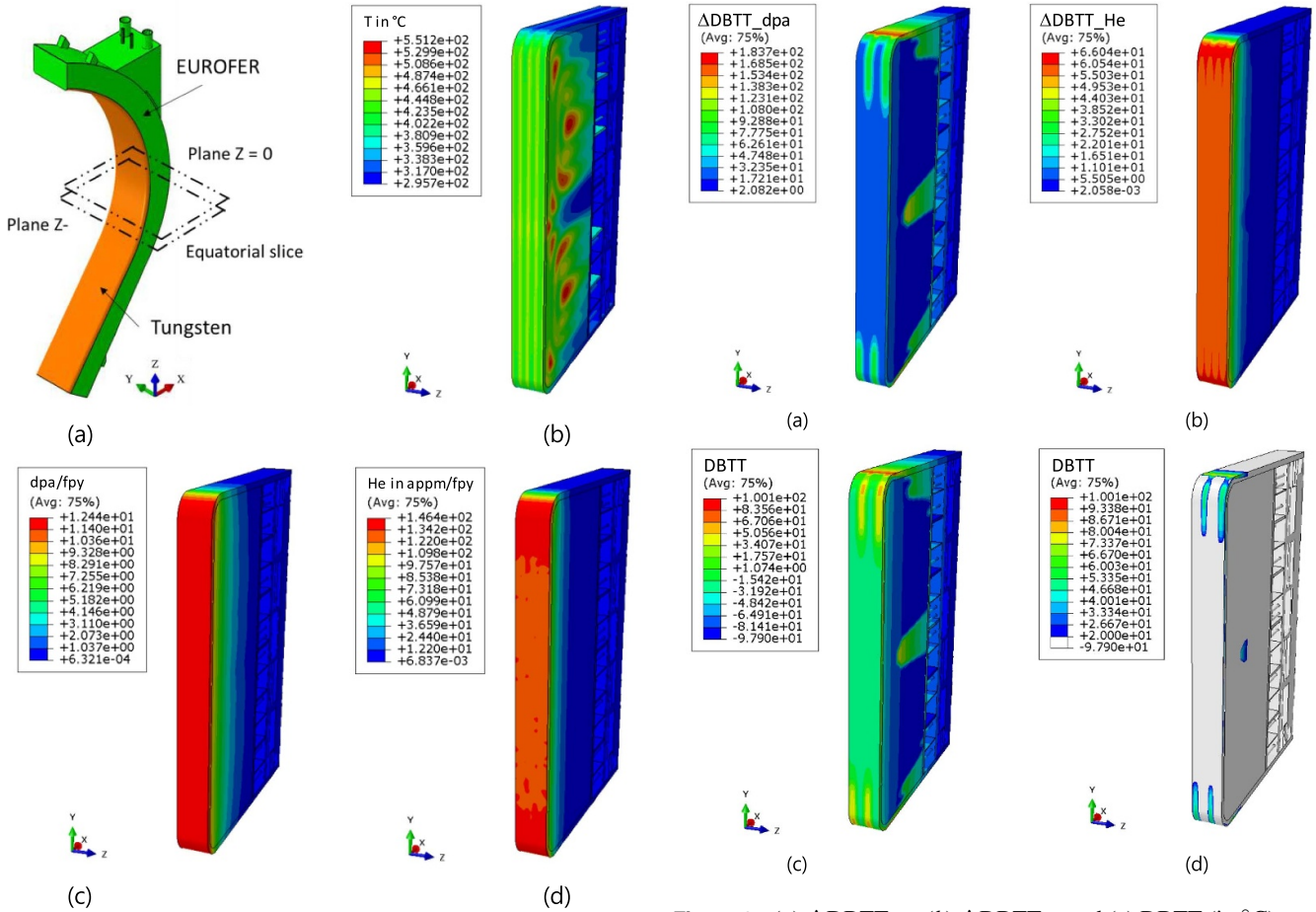


**Figure 2.** (a) WCLL blanket segment with the position of the equatorial slice. (b)–(d) Temperature, dpa rate and He generation rate distribution in the equatorial slice, respectively.

**Figure 3.** (a)  $\Delta DBTT_{dpa}$ , (b)  $\Delta DBTT_{He}$  and (c) DBTT (in °C) after 2 fpy operations in the equatorial slice of the WCLL blanket segment; (d) critically embrittled regions with DBTT greater than RT.

presence of a counter-current flow in the FW channels produces EUROFER embrittlement near the inlet channel where the structure temperature is closer to that of the coolant (i.e.  $<350\text{ }^{\circ}\text{C}$ ). One of these regions is in the middle of the plasma-facing front wall, a thin layer at a depth marking the middle of the walls between the cooling channels and spreads over the whole width of the walls (see figure 4). This layer becomes thicker and thicker towards the side walls of the FW, reaching its largest spread with respect to thickness in the side walls. On the side walls, the region covers nearly the whole cross-section of the FW (see figure 5).

To assess the critically embrittled zones, in particular, the risk of their brittle/non-ductile fracture, a fracture mechanics approach is adopted, which is described in the following section.

### 3. Approach for non-ductile fracture assessment

In the KTA 3201.2 [17] and similarly in ASME-BPV, section 3, Division 1, appendix G [18] fracture mechanical rules for design against brittle failure can be found with which the assessment is performed based on fracture toughness ductile-to-brittle transition curve and its shift due

to irradiation. The rules are mainly developed for considering irradiation-induced embrittlement of ferritic reactor vessel steels, particularly towards the end of life, where the DBTT might be shifted to temperatures higher than RT.

Starting from stress analysis results, a surface flaw in the shape of a crack perpendicular to the maximum principal stress is postulated. For this flaw, the stress intensity factor  $K_I(t, T)$  at each instant is determined and evaluated based on the reference fracture toughness  $K_{IR}(T)$ , which corresponds to the crack arrest toughness  $K_{Ia}(T)$  under which a propagating crack stops. It shall be a lower bound for all measured values of static fracture toughness  $K_{Ic}(T)$  and dynamic fracture toughness  $K_{Id}(T)$ .

For ferritic steels with minimum yield strength at RT of 345 MPa or less, the  $K_{Ic}$  and  $K_{IR}$  values are approximated by the analytical formulas (see figure 6) [17]:

$$K_{Ic} = 36.46 + 3.08 \exp[0.036(T - RT_{NDT} + 55.5)], \quad (6)$$

$$K_{IR} = 29.41 + 1.34 \exp[0.026(T - RT_{NDT} + 88.9)] \quad (7)$$

( $K_{Ic}$  and  $K_{IR}$  in  $\text{MPa}\sqrt{\text{m}}$ ,  $T$  and  $RT_{NDT}$  in K).

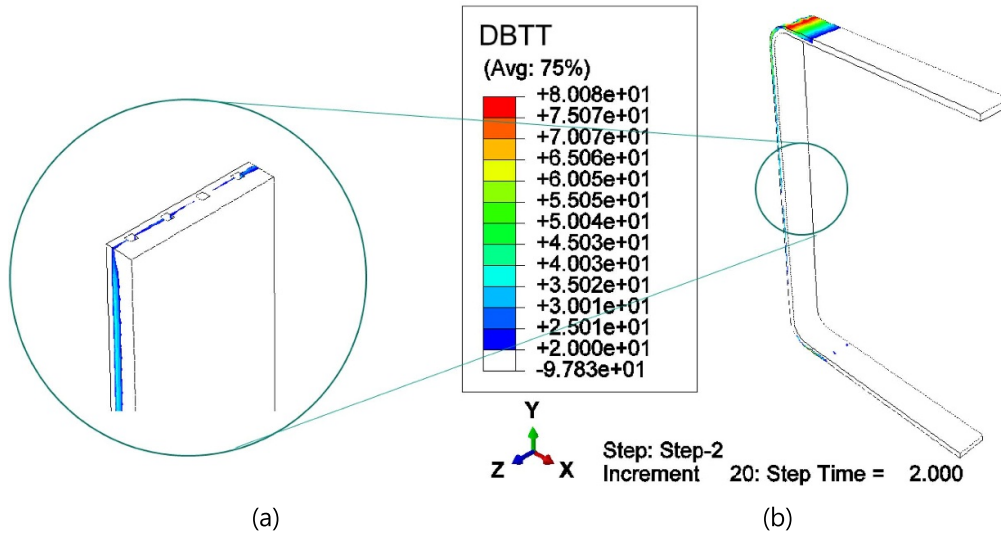


**Figure 4.** Critically embrittled region (DBTT > 20 °C) in the FW of the WCLL blanket after 2 fpy, with the zoomed-out circle showing the middle of the plasma-facing part.

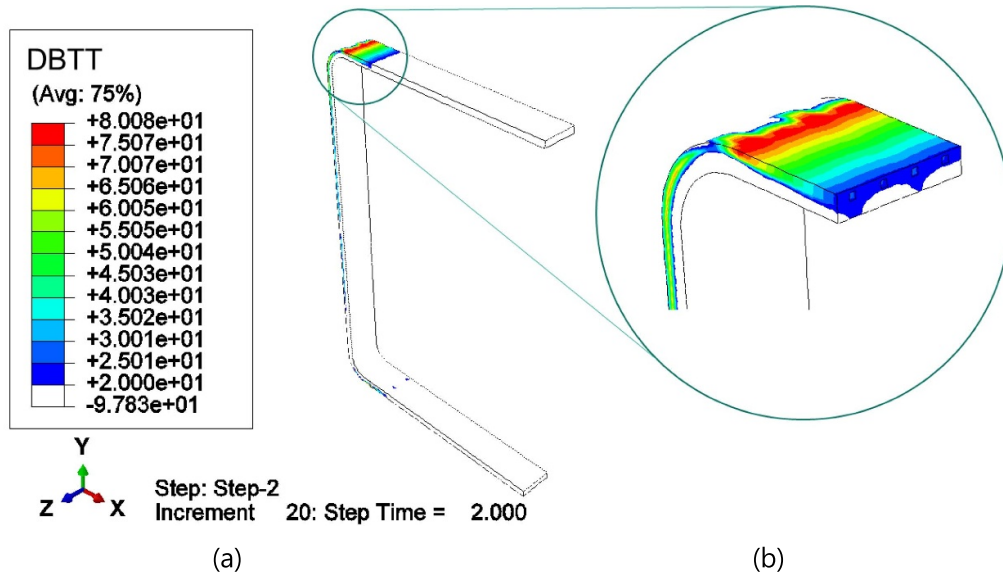


**Figure 5.** Critically embrittled region (DBTT > 20 °C) in the FW of the WCLL blanket after 2 fpy, with the zoomed-out circle showing the side wall.

$RT_{NDT}$  is the reference nil-ductility transition temperature determined considering data from Charpy impact and Pellini drop weight testing as,

$$RT_{NDT} = \max \{ T_{NDT}, T_{AV}(68 J) - 33 K, T_{AV}(0.9 mm) - 33 K \}, \quad (8)$$

with

$T_{NDT}$  nil ductility transition temperature that is the highest temperature at which a specimen breaks in drop weight experiment after Pellini,

$T_{AV}(68 J)$  temperature at which a Charpy impact energy of at least 68 J on an ISO-Vspecimen is measured,

$T_{AV}(0.9 mm)$  temperature at which a lateral deformation of at least 0.9 mm on an ISO-Vspecimen in a Charpy impact test is observed.

For materials that have specified minimum yield strengths at RT greater than 345 MPa but not exceeding 620 MPa, equation (7) may be used provided that fracture mechanics data ( $K_{Ic}$  and  $K_{Ia}$ ) are obtained on at least three heats of the material on a sufficient number of specimens to cover the temperature range of interest, including the weld metal and heat-affected zone, and provided that the data are equal to or above the values given by equation (7).

In order to consider embrittlement, e.g. due to irradiation, the embrittlement-induced temperature shift determined at the

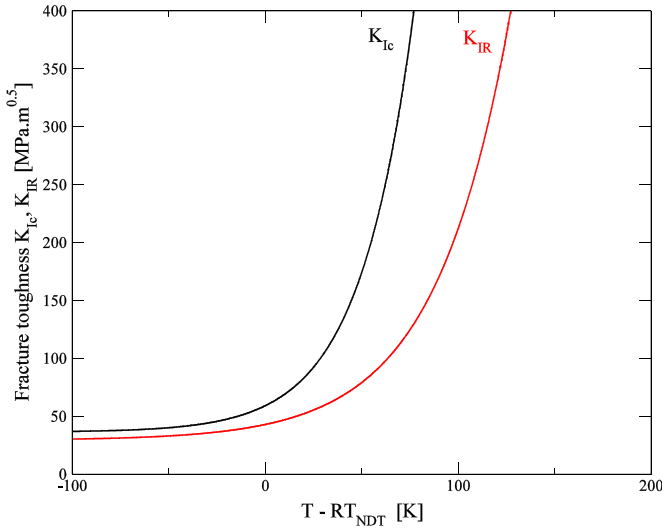


**Figure 6.** Brittle to ductile transition of static and reference fracture toughness of ferritic steels with minimum yield strength at RT of 345 MPa.

Charpy impact energy of 41 J,  $\Delta T_{41}$ , for the embrittled state is applied to equation (7) as shift in  $RT_{NDT}$  [17]:

$$K_{IR} = 29.41 + 1.34 \exp [0.026 (T - RT_{NDT} - \Delta T_{41} + 88.9)]. \quad (9)$$

The assessment is performed by

- calculating for the postulated surface crack (for loading levels A and B: 0.25 of the wall thickness in depth and 1.5 of the wall thickness in length)  $K_{I,P}$  and  $K_{I,Q}$  as the stress intensity factors resulting from primary and secondary stresses, respectively,
- applying a safety factor of 2 on  $K_{I,P}$
- and ensuring that the sum  $2K_{I,P} + K_{I,Q}$  is always below  $K_{IR}$ , particularly during start-up and shut-down (see figure 7).

For applying the approach to EUROFER structures,  $RT_{NDT}$  needs to be determined and, in case of irradiated EUROFER,  $\Delta T_{41}$  and its dependence on irradiation dose are also required. Having  $T_{AV}(68 \text{ J})$  known for EUROFER [19],  $RT_{NDT}$  is assumed to be equal to  $T_{AV}(68 \text{ J}) - 33 \text{ K}$  according to equation (8), resulting in  $RT_{NDT} = -115^\circ\text{C}$ . For irradiated EUROFER,  $\Delta T_{41}$  is assumed to be equal to the shift in DBTT. To check the applicability of the curve of the reference fracture toughness (equation (7)), the fracture toughness data available for EUROFER in the Material Properties Handbook normalized to 1T specimen [20] are plotted versus this curve as well as that of  $K_{Ic}$  (equation (6)) in figure 8. Apart from the very few data points by Bonadé (2006) and one data point by Rensman (2005), all data points are above the curve of the reference fracture toughness and, thus, on the right side to justify its applicability to EUROFER. However, due to the lack of fracture toughness data for irradiated EUROFER the applicability of the reference fracture toughness curve shifted by  $\Delta T_{41} = \Delta DBTT$  cannot be verified yet. In addition, it cannot be verified that the lower shelf fracture toughness remains unaffected by irradiation, which probably in the case

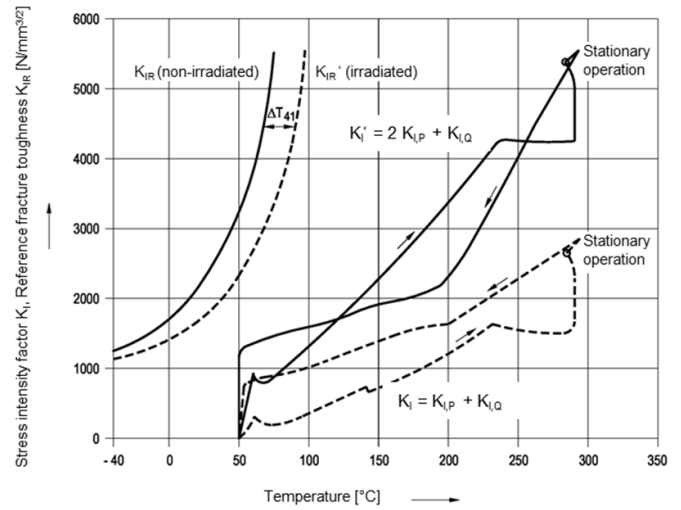


**Figure 7.** Evaluation of stress intensity factors calculated for an artificial flaw during start-up and shut-down on the base of the brittle to ductile transition curve of the reference fracture toughness. Reproduced with permission from [17]. Operational cycle is exemplary and does not correspond to that of the considered DEMO blanket.

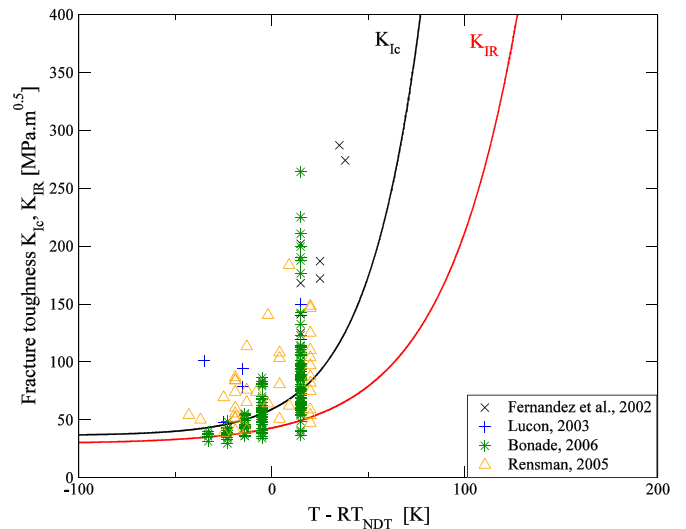


**Figure 8.** Fracture toughness data of EUROFER versus the curves of static and reference fracture toughness available in the code.

of excessive He production might not be true. However, observations on model steels indicate no substantial effect of transmuted He on lower shelf fracture toughness up to 330 appm He (see figure 9 in [12]).

In the following assessments, the postulated surface crack is part-through-wall semi-elliptical with a depth  $a$  and a length at the surface  $2c$ , as illustrated in figure 9.

For the assessment, the stress intensity factors at the depth and surface points of the 2D surface crack are calculated by applying the influence coefficient method of RCC-MRx, A16 [21] for part-through-wall semi-elliptical defects in a plate (PLA-D2DS). Therefore, the coefficients of the third-order polynomial  $\sigma_0$ ,  $\sigma_1$ ,  $\sigma_2$  and  $\sigma_3$ , representing the nominal stress normal to the plane of the crack, here the first principal stress

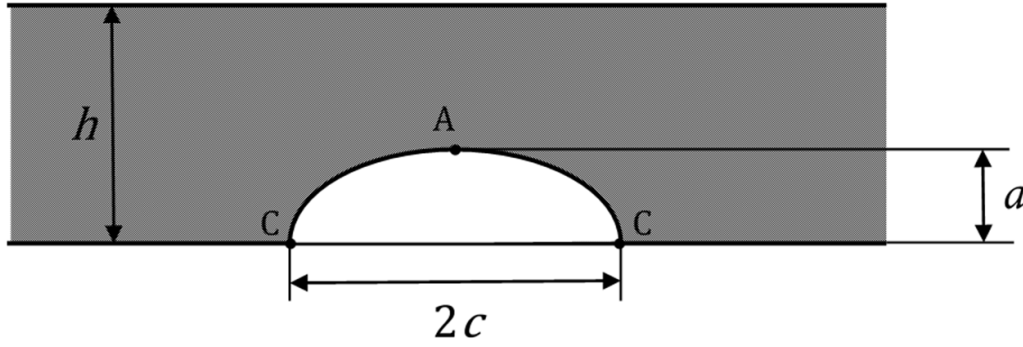


Figure 9. Geometry of the 2D surface crack postulated at the positions selected for non-ductile fracture assessment.

calculated for the crack-free structure along the considered crack depth direction, are determined:

$$\sigma\left(\frac{x}{h}\right) = \sigma_0 + \sigma_1\left(\frac{x}{h}\right) + \sigma_2\left(\frac{x}{h}\right)^2 + \sigma_3\left(\frac{x}{h}\right)^3 \quad \text{with } 0 < x < h. \quad (10)$$

Using these coefficients and the associated influence coefficients  $i_0$ ,  $i_1$ ,  $i_2$  and  $i_3$ , which depend on the crack geometry, in particular,  $a/c$  and  $a/h$  (see figure 9) and are tabulated in [21] for the depth point A and surface point C, respectively, the stress intensity factors at these two points are calculated to:

$$K_I = \left[ \sigma_0 i_0 + \sigma_1 i_1 \left(\frac{a}{h}\right) + \sigma_2 i_2 \left(\frac{a}{h}\right)^2 + \sigma_3 i_3 \left(\frac{a}{h}\right)^3 \right] \sqrt{\pi a}. \quad (11)$$

The calculated stress intensity factors at the depth and surface points are then assessed according to the procedure presented above by checking the following criteria (stresses caused by coolant pressure or maintenance loads are primary stresses):

$$2K_I^A < K_{IR}(20^\circ\text{C}, \Delta\text{DBTT}) \quad \text{and} \quad 2K_I^C < K_{IR}(20^\circ\text{C}, \Delta\text{DBTT}), \quad (12)$$

with  $\Delta\text{DBTT}$  as the shift in DBTT determined for the position of the postulated crack. Here, its maximum value in the FW after 2 fpy operation is considered. The size of the postulated crack is selected according to the codes ( $a/h = 0.25$  and  $a/c = 1/3$ ) presuming that cracks with larger sizes are not present in the structure even after 2 fpy operation. The margin to the limit, the reference fracture toughness  $K_{IR}(20^\circ\text{C}, \Delta\text{DBTT} = 180^\circ\text{C})$ , can be determined to:

$$\min\left(\frac{K_{IR}}{2K_I^A}, \frac{K_{IR}}{2K_I^C}\right) \times 100\%. \quad (13)$$

Hence, margin values higher than 100% imply that the criteria in equation (12) are fulfilled and non-ductile fracture is not expected, while values lower than 100% mean violation of at least one of the criteria in equation (12).

#### 4. Non-ductile fracture assessment in case of re-pressurization of BB

To conduct the assessment based on the approach described in the previous section considering the coolant pressure loads, the resulting stresses in the critically embrittled region need to be calculated allowing the determination of the stress intensity factors for the postulated defects at the highly loaded positions. Since the finite element mesh of the equatorial slice of the WCLL blanket segment, particularly of the FW, is coarse for reliable calculation of the stresses, a 2D model is generated for the FW cross-section with a fine mesh consisting of generalized plane strain elements. To avoid unreasonable stress peaks at the sharp corners of the channels they were rounded with a relatively small radius of 0.5 mm. The model is then loaded applying a coolant pressure of 15.5 MPa (155 bar) to the surfaces of the cooling channels. An RT of 20 °C has also been assumed. These conditions (i.e. high pressure and low temperature) are quite conservative because they maximize the primary stresses when part of the structural material is brittle. Of course, this is an extreme case because under no condition is the BB (after irradiation) expected to experience high pressure at low temperature (i.e. usually, the pressure and the temperature are increased or decreased in a combined way). The resulting field of the first (max.) principal stress is plotted in figure 10 indicating the highest stresses in the 3 mm thin outer wall of the cooling channel with stress peaks at their corners.

Based on the calculated stress distribution and the identified critically embrittled zones in the FW (see figures 4 and 5) three positions (P1-P3) are selected for conducting the non-ductile fracture assessment. These positions are indicated in figure 11 in which the postulated 2D semi-elliptical cracks as well as their orientation are illustrated. They are placed in planes perpendicular to the first principal stress direction and the plane of the model, respectively, with the red lines in figure 11 indicating their extension in the depth direction. The assessment results obtained following the approach presented in the previous section for the postulated surface crack at the positions P1-P3 are listed in table 1. In addition to the stress intensity factor at the depth and surface points, the reference fracture toughness  $K_{IR}(20^\circ\text{C}, \Delta\text{DBTT} = 180^\circ\text{C})$  is given together with the margin to it determined using equation (13).



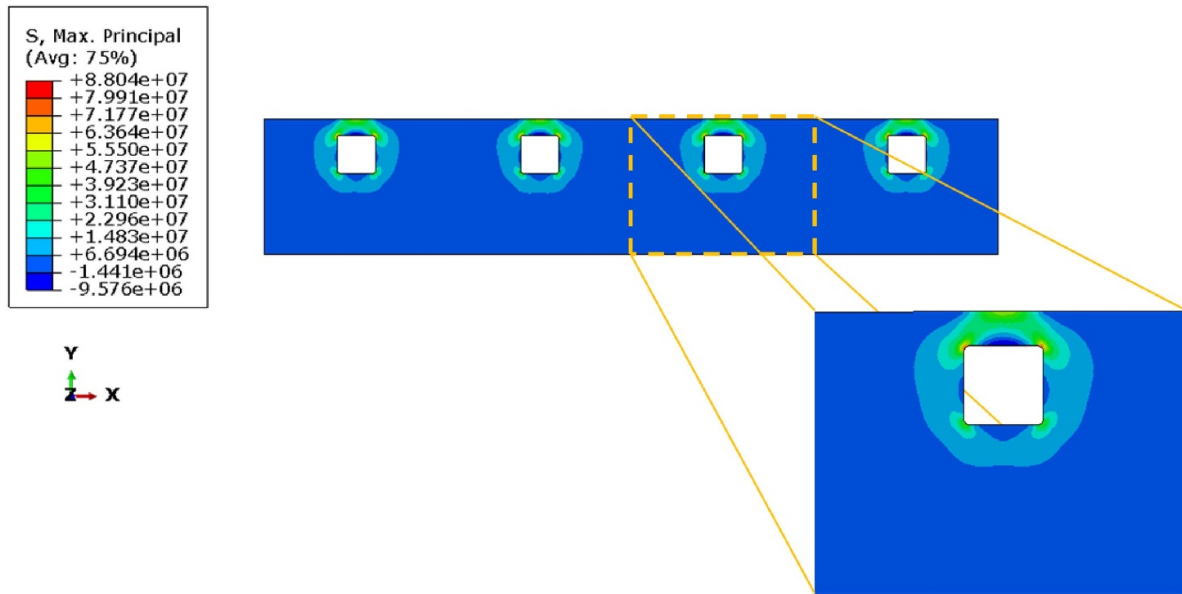


**Figure 10.** Contour plot of first principal stress resulting from coolant pressure load in the FW (in Pa).

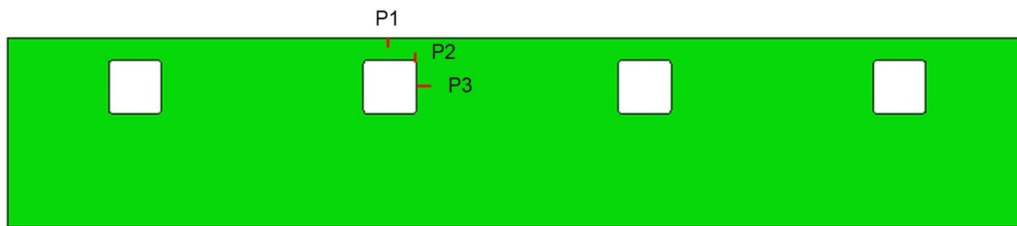


**Figure 11.** Selected positions for the non-ductile fracture assessment.

**Table 1.** Assessment results considering the postulated surface crack at the positions P1–P3 and coolant pressure load.

Position	$K_I^A$ (MPa $\sqrt{m}$ )	$K_I^C$ (MPa $\sqrt{m}$ )	$K_{IR}$ (MPa $\sqrt{m}$ )	Margin (%)
P1	2.196	1.652	33.617	765
P2	2.930	2.590	33.617	574
P3	1.227	1.012	33.617	1370

Since the margin values are higher than 100%, non-ductile fracture is not expected for all considered positions in this assessment (see table 1). Coolant pressure load yields relatively low stresses that do not cause non-ductile failure of the FW after 2 fpy operation based on the conducted assessment and the assumptions made herein. Among the positions assessed, P2, which is located at the corner of the cooling channel on the thin wall side (see figure 11), is the most critical one. Increasing the radius at these corners would reduce the highest stresses appearing there and thus the risk of non-ductile fracture, e.g. in the case of transient overpressure of the incompressible coolant.

## 5. Non-ductile fracture assessment in case of lifting the BB segment

In order to determine the critically loaded parts of the WCLL blanket during maintenance, in particular, when lifting the

banana-shaped blanket segment (see figure 2(a)) and moving it out of the vessel, the stresses calculated in proper finite element simulations performed on a rough model of this segment—without cooling channels—are analyzed. In these simulations, three loading scenarios/cases (LC) were considered:

- LC1: 1 Dead weight of the segment without lithium-lead (LiPb), which is supposed to be drained out of it before starting the maintenance procedure
- LC1: 2 Dead weight of the segment without lithium-lead (LiPb) plus seismic loads originating from the acceleration of the component up and sideways [22]
- LC1: 3 Dead weight of the segment with lithium-lead (LiPb), i.e. undrained

In view of fracture mechanical assessment, the maximum (first) principal stresses appearing in the FW due to the

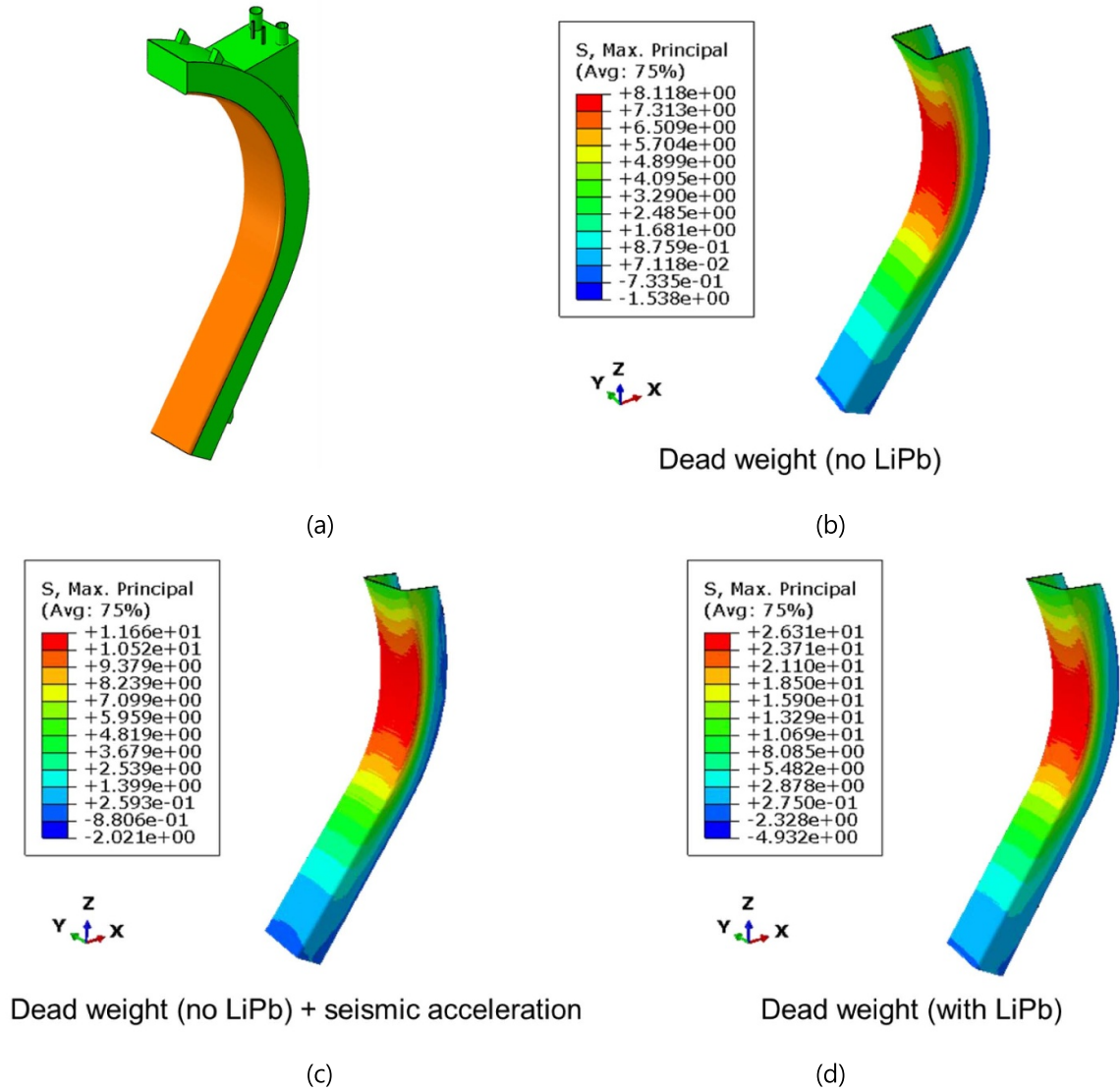


**Figure 12.** (a) Rough model of the banana-shaped WCLL blanket segment; (b) to (d) contour plot of maximum (first) principal stresses in the FW of the WCLL blanket segment due to dead weight without LiPb, dead weight without LiPb plus seismic acceleration, and dead weight with LiPb, respectively (in MPa).

considered three load cases are evaluated to identify the positions most critical with respect to crack initiation and propagation. The contour plots in figures 12(b)–(d) make clear that this position for all three load cases is in the front part of the FW at the equatorial surface area. Quantitatively the seismic acceleration (LC2) and the weight of LiPb (LC3) increased the stresses by  $\approx 44\%$  and  $\approx 224\%$ , respectively. Indeed, the maintenance loads pull the whole banana-shaped structure in the vertical direction and straighten it with a bending moment having its maximum at the equatorial cross-section of the FW.

In a first step, a fracture mechanical assessment was performed following the approach for non-ductile fracture assessment presented above by considering and evaluating a postulated 2D surface crack at the identified most critical position lying in the equatorial cross-section of the FW (see figure 13). The 2D surface crack is located on the outer (i.e. plasma

facing) side of the FW. The depth  $a$  and length  $2c$  of the crack are given by the adopted approach to 0.25 and 1.5 of the wall thickness  $h$  (see figure 13). With  $h = 25$  mm for the rough model without cooling channels at the selected position  $a$  and  $2c$  are calculated to 6.25 and 37.5 mm, respectively.

The assessment results for the postulated surface crack are listed in table 2. In addition to the stress intensity factors at the depth and surface points the reference fracture toughness  $K_{IR}$  ( $20^\circ\text{C}$ ,  $\Delta\text{DBTT} = 180^\circ\text{C}$ ) is given together with the margin to it determined using equation (13).

For an FW without cooling channels, the margin values are far higher than 100%. Hence, non-ductile fracture is not expected for all considered load cases (see table 2). LC3 yields the highest stresses and consequently the lowest margin.

The assessment was continued considering an FW with cooling channels. To calculate stresses within the front wall, a submodel was created by cutting an equatorial slice out of

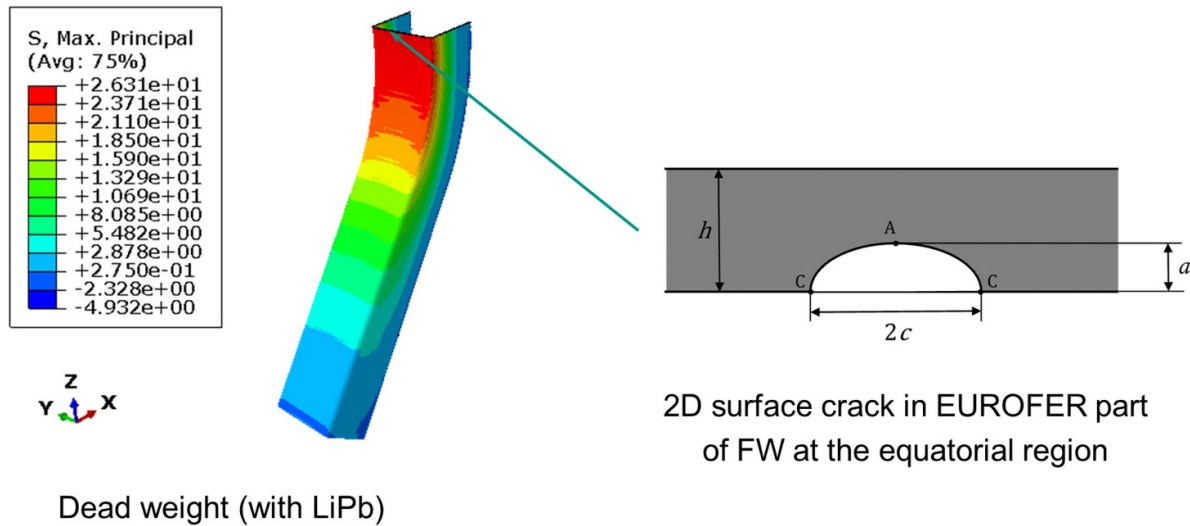


**Figure 13.** Stress in most critical position in the EUROFER part of the FW (in MPa, left) and geometry of the part-throughwall semi-elliptical surface crack (right) considered for the fracture mechanical assessment (crack plane perpendicular to the  $z$  direction).

**Table 2.** Assessment results considering the postulated surface crack at the identified most critical position of the FW during maintenance.

Load case	$K_I^A$ (MPa $\sqrt{m}$ )	$K_I^C$ (MPa $\sqrt{m}$ )	$K_{IR}$ (MPa $\sqrt{m}$ )	Margin (%)
LC1	1.047	0.683	33.617	1605
LC2	1.515	0.989	33.617	1110
LC3	3.388	2.212	33.617	496

the rough global model of the banana-shaped blanket segment and importing it in Abaqus as a part. Using another Abaqus part representing the cooling channels and the Abaqus CAE tool for merging/cutting parts, a submodel for the FW with cooling channels was generated. Indeed, three submodels were prepared following this procedure with a front wall thickness of 3, 4 and 5 mm, respectively. Each of the submodels was then appropriately meshed and loaded by linking it with the global model using the node-based submodeling technique.

In the Abaqus simulations for the submodel with 3 mm front wall thickness, the wall thickness in the current reference design, and the loads due to LC1, LC2 and LC3 were respectively considered by selecting the corresponding global model result file. Figure 14 shows the obtained results for load cases LC1–LC3, in particular, the contour plots for the maximum (first) principal stress in the region of the cooling channel closest to the equatorial plane of the banana-shaped blanket segment. As expected, the values are significantly higher than those calculated for the model without cooling channels, with the highest values appearing at the corners of the rectangular-shaped cooling channel.

A fracture mechanical assessment as conducted on the rough global model of the FW was then performed for the submodel considering the strongly reduced front wall thickness in the region of the cooling channels. Similarly, a part-throughwall semi-elliptical crack with a depth  $a$  and length  $2c$  equal to 0.25 and 1.5 of the wall thickness  $h$ , respectively, as prescribed by the adopted approach, was assumed at

position P1, at the front surface penetrating in a plane parallel to the equatorial cross-section (see figure 15) and evaluated considering the same methodology. Since the maximum first principal stress appears at the corner in the cooling channel, another site for the crack P2 is considered at which the crack is placed at the corner of the cooling channel with penetration direction towards the front surface in a plane parallel to the equatorial cross-section (see figure 15).

The results of the assessment are listed in table 3 for both positions and reveal that the criteria for non-ductile fracture are not violated by the considered maintenance loads. Moreover, the calculated margins are comfortable indicating that ensuring flaw sizes smaller than the crack sizes considered in this work, no risk of non-ductile fracture is given by the maintenance loads. Among the positions assessed, P2, which is located at the corner of the cooling channel on the thin wall side (see figure 15), is the more critical one. For this position, the crack depth  $a$  and its length  $2c$  were systematically varied determining the critical/maximum tolerable crack sizes ( $a^*$ ,  $2c^*$ ) for which the maximum maintenance load (LC3) would not yield non-ductile fracture according to the criteria. Thereby, the crack depth  $a$  was incrementally reduced, starting with a depth equal to 80% of the wall thickness, and for each reduced crack depth  $a^*$  the crack length  $2c$  was incrementally increased and for each such resulting crack geometry the stress intensity factors at the apexes of the crack were calculated and checked by the criteria in equation (12). The maximum crack length for which the criteria are not violated is then declared to  $2c^*$ , etc. In figure 16, the results are plotted in a  $2c^*$  versus  $a^*$

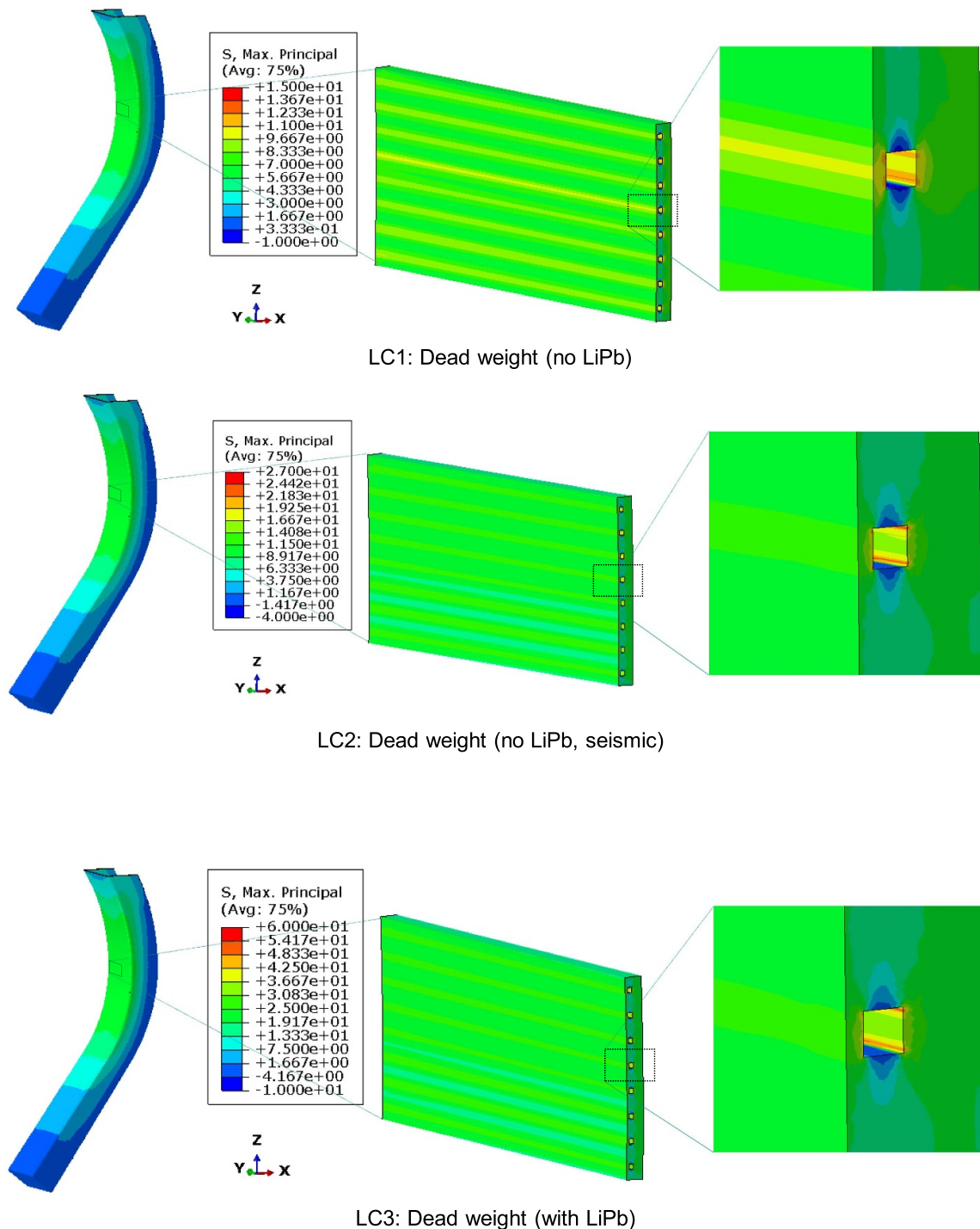


**Figure 14.** Contour plots of maximum (first) principal stresses in the FW submodel with cooling channels and 3 mm front wall thickness due to dead weight without LiPb (LC1), dead weight without LiPb plus seismic acceleration (LC2), and dead weight with LiPb (LC3), respectively (in MPa).

diagram in which the smaller the depth  $a^*$  the larger the length  $2c^*$  is. However, the values of both are quite high, which indicates once more that the maintenance loads are obviously not too high to cause fracture provided that large cracks/flaws are timely detected and repaired.

To assess whether geometry changes in the FW design, in particular, the thickness of the front wall would increase

the margin to the risk of non-ductile fracture due to maintenance loads, the other submodels with 4 and 5 mm front wall thicknesses were used to resolve the stresses in the front wall by conducting Abaqus simulations considering the load case with the highest loads (LC3). For fracture mechanical assessment and according to the adopted approach, a part-throughwall semi-elliptical crack with a depth  $a$  and

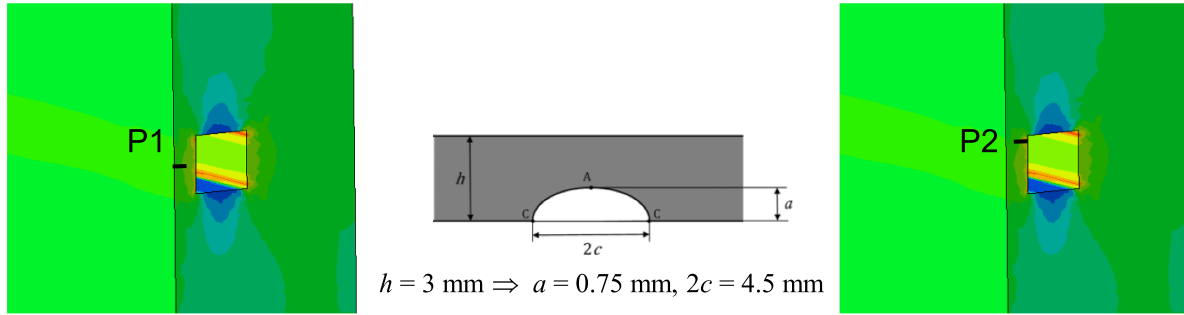


**Figure 15.** Most critical positions P1 and P2 in the EUROFER part of the FW with cooling channels and the geometry of the part-throughwall semi-elliptical surface crack considered for the fracture mechanical assessment.

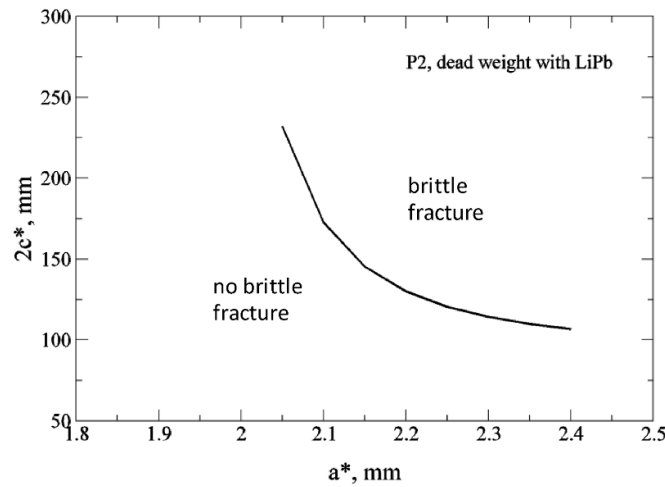


**Figure 16.** Maximum tolerable crack sizes ( $a^*$ ,  $2c^*$ ) for the position P2 of the FW with cooling channels under maintenance loads (LC3).

**Table 3.** Assessment results considering the postulated surface crack at the identified most critical positions P1 and P2 of the FW with cooling channels during maintenance.

Position	Load case	$K_I^A$ (MPa $\sqrt{m}$ )	$K_I^C$ (MPa $\sqrt{m}$ )	$K_{IR}$ (MPa $\sqrt{m}$ )	Margin (%)
P1	LC1	0.521	0.332	33.617	3229
	LC2	0.659	0.411	33.617	2551
	LC3	1.423	0.887	33.617	1182
P2	LC1	0.623	0.422	33.617	2699
	LC2	0.885	0.620	33.617	1899
	LC3	1.910	1.338	33.617	880

**Table 4.** Assessment results considering the postulated surface crack at the identified most critical position P2 of the FW with cooling channels and different front wall thicknesses under the highest maintenance loads (LC3).

Wall thickness mm	$K_I^A$ (MPa $\sqrt{m}$ )	$K_I^C$ (MPa $\sqrt{m}$ )	$K_{IR}$ (MPa $\sqrt{m}$ )	Margin (%)
3	1.910	1.338	33.617	880
4	2.023	1.235	33.617	831
5	2.274	1.550	33.617	739

length  $2c$  equal to 0.25 and 1.5 of the wall thickness  $h$ , was respectively assumed at position P2, the position with the smallest margin (see table 3). The results of this assessment are listed in table 4 and show that despite the stresses being reduced (see figure 17) the margin slightly decreases with increasing wall thickness, which mainly has

to do with the fact that the considered crack size also increases with wall thickness, overcompensating the reduction of stresses.

As was done for the standard design with 3 mm front wall thickness, the critical/maximum tolerable crack sizes ( $a^*$ ,  $2c^*$ ) for which the maximum maintenance loads (LC3) would

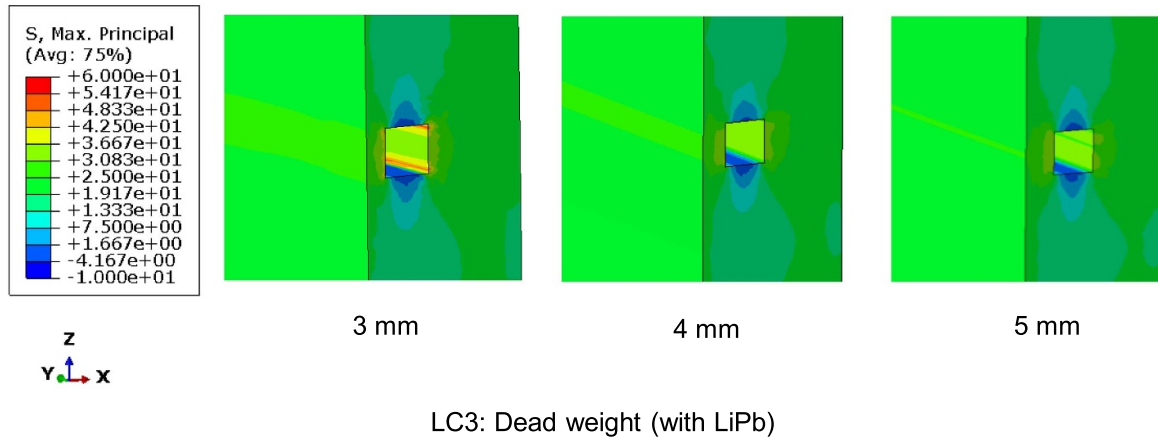


**Figure 17.** Reduction of stresses due to load case LC3 in the FW front wall by increasing its thickness.

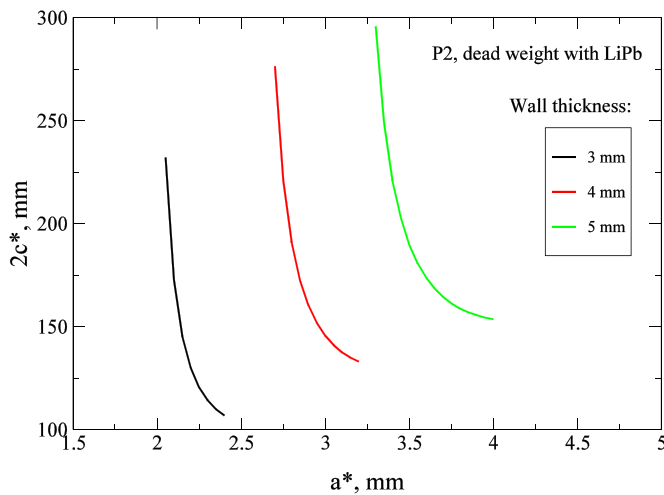


**Figure 18.** Maximum tolerable crack sizes ( $a^*$ ,  $2c^*$ ) for the position P2 of the FW with cooling channels and different front wall thicknesses under maintenance loads (LC3).

not yield non-ductile fracture according to the criteria are calculated for the other front wall thicknesses and position P2. In figure 18, the results are plotted for the different front wall thicknesses in a  $2c^*$  versus  $a^*$  diagram. These results clearly demonstrate that larger cracks/flaws are tolerable when increasing the front wall thickness, which is certainly an option in case the detection of cracks/flaws by non-destructive testing is limited to sizes larger than those tolerable in the standard design. In addition, initially small cracks/flaws may propagate during operation by fatigue crack growth (FCG), particularly under the envisaged pulsed operation, and reach sizes larger than those tolerable in the standard design. Hence, considering FCG in the assessment of detectable cracks/flaws is an important step that is already planned in future activities.

## 6. Conclusion

The embrittlement of WCLL BB was investigated quantifying the locally resolved DBTT shift and identifying the 3D spread of critically embrittled zones, in particular, those with DBTT

shifted to temperatures above RT. Therefore, a suitable, not overly conservative procedure was derived based on current knowledge on the embrittlement behaviour of EUROFER under neutron irradiation considering dpa and transmuted He effects. It requires as input the temperature, dpa and He generation rates during operation. These were determined based on relevant analyses of the BB and applicable procedures.

To assess the risk of brittle/non-ductile fracture in the critically embrittled zones, a fracture mechanical approach established in existing design codes for embrittled ferritic structures is adapted to the embrittled EUROFER structures, making proper assumptions with respect to missing material properties and size of the reference flaw to be considered.

The stresses in the BB segment were assessed in states when it is rather cold, i.e. during maintenance phases. According to the criteria of the approach adopted for non-ductile fracture assessment, coolant pressure as well as loads when lifting the BB segment were not found to be high enough to cause fracture in the FW. The calculated comfortable margin to the criteria resulted in relatively high maximum tolerable crack sizes. These were determined in case of the lifting of the BB segment in a parameter study for different FW front wall thicknesses, demonstrating that with respect to these loads larger cracks/flaws can be tolerated in thicker FW front walls whose size, however, needs to be confirmed prior to maintenance, e.g. by inspecting the FW before initial installation and assessing the extension of detected flaws during operation by a dedicated FCG analysis.

## Acknowledgments

This work has been carried out within the framework of the EUROfusion Consortium, funded by the European Union via the Euratom Research and Training Programme (Grant Agreement No. 101052200—EUROfusion). Views and opinions expressed are however those of the author(s) only and do not necessarily reflect those of the European Union or the European Commission. Neither the European Union nor the European Commission can be held responsible for them.

## ORCID iDs

Jarir Aktaa  <https://orcid.org/0000-0002-0891-5331>  
 Pietro Arena  <https://orcid.org/0000-0002-2860-4717>  
 Gandolfo Alessandro Spagnuolo  <https://orcid.org/0000-0001-8416-3349>

## References

- [1] Martelli E., Giannetti F., Caruso G., Tarallo A., Polidori M., Barucca L. and Del Nevo A. 2018 Study of EU DEMO WCLL breeding blanket and primary heat transfer system integration *Fusion Eng. Des.* **136** 828–33
- [2] Cismondi F. et al 2018 Progress in EU breeding blanket design and integration *Fusion Eng. Des.* **136** 782–92
- [3] Gaganidze E. 2007 *Assessment of fracture mechanical experiments on irradiated EUROFER97 and F82H specimens* FZKA 7310 Karlsruhe Institute of Technology (KIT) (<https://doi.org/10.5445/IR/270068448>)
- [4] Gaganidze E. and Aktaa J. 2013 Assessment of neutron irradiation effects on RAFM steels *Fusion Eng. Des.* **88** 118–28
- [5] Arena P. et al 2021 The DEMO water-cooled lead–lithium breeding blanket: design status at the end of the pre-conceptual design phase *Appl. Sci.* **11** 11592
- [6] Werner C.J. et al 2018 MCNP (version 6.2) release notes *Report LA-UR-18-20808* Los Alamos National Laboratory (<https://doi.org/10.2172/1419730>)
- [7] Nuclear Energy Agency 2018 *JEFF3.2 Nuclear Data Library* (available at: [www.oecd-nea.org/dbforms/data/eva/evatapes/jeff\\_32/](http://www.oecd-nea.org/dbforms/data/eva/evatapes/jeff_32/))
- [8] Spagnuolo G.A., Chiovaro P., Di Maio P.A. and Favetti R. 2019 A multi-physics integrated approach to breeding blanket modelling and design *Fusion Eng. Des.* **143** 35–40
- [9] Favetti R., Chiovaro P., Di Maio P.A. and Spagnuolo G.A. 2020 Validation of multi-physics integrated procedure for the HCPB breeding blanket *Int. J. Comput. Methods* **17** 1950009
- [10] Spagnuolo G.A. 2020 Integrated multi-physics design tool for fusion breeding blanket systems—development and validation *PhD Thesis* Karlsruhe Institute of Technology (KIT) (<https://doi.org/10.5445/IR/1000123701>)
- [11] Edemetti F., Di Piazza I., Del Nevo A. and Caruso G. 2020 Thermal-hydraulic analysis of the DEMO WCLL elementary cell: BZ tubes layout optimization *Fusion Eng. Des.* **160** 111956
- [12] Wakai E. et al 2005 Radiation hardening and -embrittlement due to He production in F82H steel irradiated at 250 °C in JMTR *J. Nucl. Mater.* **343** 285–96
- [13] Gaganidze E. and Aktaa J. 2013 *Issues Related to Radiation on Blanket and Divertor Materials* EFDA\_D\_2KXQA6 EUROfusion
- [14] Rieth M., Dafferner B. and Röhrig H.-D. 1998 Embrittlement behaviour of different international low activation alloys after neutron irradiation *J. Nucl. Mater.* **258** 1147–52
- [15] Dai Y. and Wagner W. 2009 Materials researches at the Paul Scherrer Institute for developing high power spallation targets *J. Nucl. Mater.* **389** 288–96
- [16] Materna-Morris E., Möslang A., Schneider H.-C. and Rolli R. 2008 Microstructure and tensile properties in reduced activation 8–9%Cr steels at fusion relevant He/dpa ratios, dpa rates and irradiation temperatures *22nd IAEA Fusion Energy Conf. (Geneva, Switzerland, 13–18 October)* pp FT/P2–2
- [17] Kerntechnischer Ausschuss (KTA) 2000 *Sicherheitstechnische Regeln des KTA, Komponenten des Primärkreises von Leichtwasserreaktoren, Auslegung, Konstruktion und Berechnung* KTA 3201.2
- [18] ASME 2010 *ASME Boiler and Pressure Vessel Code, Section III, Division 1, Appendix G*
- [19] Rieth M., Schirra M., Falkenstein A., Graf P., Heger S., Kempe H., Lindau R. and Zimmermann H. 2003 *EUROFER97 - Tensile, Charpy, Creep and Structural Tests* FZKA 6911 Karlsruhe Institute of Technology (KIT) (<https://doi.org/10.5445/IR/270055720>)
- [20] Gaganidze E. 2020 *Material Property Handbook EUROFER97* EFDA\_D\_2NZHBS EUROfusion
- [21] AFCEN 2015 *RCC-MRx Code, section III, Tome 1, Subsection Z, A16*
- [22] Bachmann C., Gliss C., Janeschitz G., Steinbacher T. and Mozzillo R. 2022 Conceptual study of the remote maintenance of the DEMO breeding blanket *Fusion Eng. Des.* **177** 113077